Surface Acoustic Waves to Control Droplet Impact onto Superhydrophobic and Slippery Liquid-Infused Porous Surfaces

Mehdi H. Biroun,[a,b,$] Luke Haworth,[a,$] Prashant Agrawal,[a] Bethany Orme,[a] Glen McHale,[c] Hamdi Torun,[a] Mohammad Rahmati,[a] YongQing Fu [a,]*

[a] Faculty of Engineering and Environment, University of Northumbria, Newcastle upon Tyne NE1 8ST, UK

[b] Department of Chemical Engineering, University College London, Torrington Place, London WC1E 7JE, UK

[c] Institute for Multiscale Thermofluids, School of Engineering, University of Edinburgh, Kings Buildings, Edinburgh EH9 3FB, UK

[$] MHB and LH contributed equally to this paper.

Keywords**:** Surface acoustic wave, SLIPS, Superhydrophobic, Droplet impact, Contact time, Impact regime

Abstract: Superhydrophobic coatings and slippery liquid infused porous surfaces (SLIPS) have shown their potentials in self-cleaning, anti-icing, anti-erosion, and anti-biofouling applications. Various studies have been done on controlling the droplet impact on such surfaces using passive methods such as modifying the lubricant layer thickness in SLIPS. Despite their effectiveness, passive methods lack on-demand control over the impact dynamics of droplets. This paper introduces a new method to actively control the droplet impact onto superhydrophobic and SLIPS surfaces using surface acoustic waves (SAWs). In this study, we designed and fabricated SLIPS on ZnO/Aluminum thin-film SAW devices and investigated different scenarios of droplet impact on the surfaces compared to those on similar superhydrophobic-coated surfaces. Our results showed that SAWs have insignificant influences on the impact dynamics of a porous and superhydrophobic surface without an infused oil layer. However, after infusion with oil, SAW energy could be effectively transferred to the droplet, thus modifying its impact dynamics onto the superhydrophobic surface. Results showed that by applying SAWs, the spreading and retraction behaviors of the droplets are altered on the SLIPS surface, leading to a change in droplet impact regime from deposition to complete rebound with altered rebounding angles. Moreover, the contact time was reduced up to 30% when applying SAWs on surfaces with an optimum oil lubricant thickness of ~8 μm. Our work offers an effective way of applying SAW technology along with SLIPS to effectively reduce the contact time and alter the droplet rebound angles.

Introduction

Understanding droplet impact behavior onto various surfaces is crucial for a wide range of applications, including 3D and inkjet printing, combustion, spray cooling, anti-icing surfaces, agriculture, forensic assay, and coating processes [1–6]. Different factors for controlling droplet impact dynamics on various surfaces have been extensively investigated, including impact regime, contact time (CT), maximum spreading radius, and rebounding angle [7,8]. Advances in smart materials, micro and nanoscale structures, and surface fabrication techniques have led to passive surface modification methods that can be used to modify surfaces for different applications [9–14]. For example, hydrophilic surfaces have been made to maximize the contact area upon impact, desirable for coating, flash cooling, and ink-jetting applications [15,16]. On the other side of the spectrum, superhydrophobic surfaces are used for anti-icing and anti-erosion applications to reduce the solid-liquid contact time during droplet impact [17–20]. However, various problems have been reported for these surfaces, such as three-phase contact line (TPCL) pinning, poor mechanical resilience, degradation of wetting properties over time, or low transparency [21–24]. Inspired by the Nepenthes pitcher plant structure, slippery liquid-infused porous surfaces (SLIPS) have been developed to achieve highly smooth and pinning-free surfaces [25,26]. SLIPS can be manufactured by imbibing porous and superhydrophobic nanostructures with a lubricating liquid (typically oil) which preferentially wets the solid and is immiscible to the contacting liquid of interest [25]. These surfaces benefit self-cleaning and anti-icing applications as they can reject various impacting liquids, not exclusively water-based [25,27,28]. Besides, as long as the lubricant is present and coats the top of the porous medium, SLIPS's properties are expected to be sustained [29]. Following these advantages, SLIPS have been effectively demonstrated for liquid mass transport [26,27,30–32].

One of the first studies of droplet impact on SLIPS was carried out by Lee et al. [33], who investigated the effects of the lubricant viscosity and the Weber number (We) (i.e., $we = \frac{\rho U_0^2 D_0}{\gamma}$, where $\rho, U_0, D_0, and\ \gamma$ are the density, impact velocity, initial diameter, and surface tension of the droplet, respectively) on the impact dynamics. They reported that a droplet's rebound and splash depend on the lubricant's viscosity. Hao et al. [34] investigated the effects of lubricant viscosity and thickness, as well as the surface roughness of substrate on droplet impact dynamics, and tuned the droplet impact by varying variables of SLIPS structures such as lubricant thickness and surface structure. Kim et al. [35] further studied the effect of the lubricating layer's viscosity on water droplet impact and showed that the maximum spreading diameter could be modified by changing the liquid viscosity. Muschi et al. [29] controlled the lubricant layer thickness by changing the rotational velocity of spin-coating and showed that a sufficiently thick lubricant layer is necessary to prevent dewetting spots on the impacted area. Kim et al. [36] compared the impact dynamics of droplets on various surfaces, including SLIPS. Their results showed that, while rough surfaces promote droplet instabilities during the spreading, lubricant infusion on the surface damps the droplet's interfacial vibrations during its spreading and retraction phases. Baek et al. [37] showed that surface tension and viscosity play important roles in droplet impact dynamics, and liquid viscosity and surface tension are the control parameters to change the maximum spreading radius and contact time.

So far, most studies on modification and control of the droplet impact on a solid surface have been carried out using passive methods such as surface texturing, superhydrophobic treatments, and lubricant infusion, such as SLIPS. Only a few active methods have been introduced to control the droplet impact dynamics, for example, utilizing electric fields [38], mechanical vibration [39,40], and ultrasonics [41]. Integration of these active methods with passive surface treatment methods may be necessary for optimal control of droplet impact on solid surfaces.

Recently, surface acoustic wave (SAW) technology has become an important platform for a wide range of microfluidic applications and droplet manipulation [42], including droplet transportation, jetting, atomization, heating, and internal streaming [43–46]. Thin film-based SAWs can be realized on many substrate materials, including silicon, glass, and metals such as aluminum (Al), thus creating opportunities for a wide range of sensing and microfluidic applications [42]. SAWs can be generated at a location remote from the impact point, and the waves can propagate to the desired area where they could be used to alter the impact behavior. SAW generation and propagation can be done on various surfaces, including flexible and bendable surfaces using thin-film technology [47]. SAWs can be switched on and off and controlled by modulating the excitation power. Moreover, it is possible to select their propagation directions across a solid surface. They have shown potential benefits for reducing droplet contact time when a droplet is impacted onto a hydrophobic surface [48,49].

This paper investigates the potential for using SAWs to manipulate and control the droplet impact on SLIPS actively. We designed and fabricated thin-film ZnO/Al SAW devices whose surfaces were made superhydrophobic by coating with hydrophobic nanoparticles and then impregnating with silicone oil to convert the surface into SLIPS. Experiments of droplet impact on these superhydrophobic and SLIP surfaces with and without the presence of SAWs were carried out, and the effects of SAWs on the impact rebound regime, contact time, rebound direction, and maximum spreading radius were systematically studied.

Experimental methods

2.1. SAW device fabrication and characterization

ZnO films (with a thickness of ~5 μm) were deposited onto (100) aluminum plates using a direct-current (DC) magnetron sputter system (NS3750, Nordiko). During deposition, the sputter chamber was maintained at a pressure of ~ 0.35 Pa, with an Ar/O_2 flow ratio of 2/3. Interdigital transducers (IDTs) composed of Cr/Au layers (with thicknesses of 20/100 nm) were fabricated onto the substrate using a standard photolithography and lift-off process. The IDTs were bidirectional and consisted of 30 pairs of fingers, with an aperture of 5 mm and a spatial periodicity of 300 μm. The resonant frequency and amplitude of the SAW devices were measured using a network analyzer (Keysight, FieldFox N9913A). The Rayleigh waves were generated on the thin film SAW devices by applying RF signals to the IDTs using a signal generator (Marconi 2024, Plainview, USA) and amplified using an RF power amplifier (Amplifier research, 75A250, Souderton, USA).

2.2. Surface treatments and characterization

To render the device's surface superhydrophobic, chemically functionalized silica nanoparticles suspended in isopropanol (Glaco^{TM} Mirror Coat "Zero" from Soft99 Co) were coated onto the surface of the SAW devices, using a process reported in Ref. [50] (See Figure 1(a)). These particles were sprayed onto the surface five times in this process, resulting in a porous network of approximately 2 μm in thickness [50,51]. After each spray coating, the surface was dried using compressed air to aid the solvent evaporation.

The porous nanoparticle structure was then infused with a liquid lubricant to convert the superhydrophobic surfaces into SLIPS. As the superhydrophobic coating used was oleophilic, the lubricant was easily wetted and diffused into the porous structure. Silicone oil (Sigma Aldrich)

with a viscosity of 20 cSt and a surface tension, γ, of 19.8 mN/m was selected as the lubricant for imbibing. A dipping robot (Fisnar F4200N) was programmed to withdraw the nanoparticle-coated surface at controlled speeds from a bath of silicone oil to control the thickness of the lubricant layer. The Landau-Levich-Derjaguin equation ($h_o = 0.94\,\alpha\,Ca^{2/3}$, where Ca is the capillary number and α capillary length) [52,53] was used to estimate the thickness of the lubricant layer. In total, four withdrawal speeds were used for the lubricant layers, e.g., 0.1 mm/s, 0.5 mm/s, 1.0 mm/s and 1.5 mm/s, producing oil thicknesses varying from 3.0 ± 0.2 µm, 8.7 ± 0.2 µm, 13.8 ± 0.2 µm to 18 ± 0.2 µm. The thickness of the thinnest lubricant layer used in the experiments was about 1.9 µm ± 0.2 µm [54] and was equivalent to the nanoparticle layer's thickness (i.e., a conformal SLIPS) [54]. To calculate the porosity of this nanoporous layer, the coated substrate is imbibed with silicone oil and rinsed under running water for at least 30 seconds to obtain a conformal silicone oil coating on the substrate. The difference in the weight of the sample before and after this oil imbibition process provides the volume of oil present in the pores (considering a density of 995kg/m3). The porosity of the nanoparticle layer is obtained experimentally as 0.57±0.15.

The surfaces were characterized using a drop shape analyzer (Krüss DSA 30). Measurements of static contact angles, θ, and contact angle hysteresis, $\Delta\theta_H$, (i.e., the difference between advancing and receding contact angles) were performed using droplets of deionized water (with a volume of 2 µl). For hysteresis measurements, a 2 µl droplet was placed onto the surface and subsequently inflated by 4 µl, left to settle for 10 seconds before being deflated. The advancing contact angle, θ_{adv}, (e.g., the largest possible angle achievable on the surface before contact line motion) was extracted from the inflation procedure, and the receding contact angle, θ_{rec}, (e.g., the smallest contact angle achievable on the surface prior to contact line motion) was obtained from the deflation step. Table 1 lists the measured data from the samples with different surface treatments.

Table 1: Key features of the fabricated surfaces for this study

	Surface type	Infused lubricant thickness (µm)	Static contact angles θ (O)	Advancing contact angle θ_{adv} (O)	Receding contact angle θ_{rec} (O)	Sliding angle θ_{SA} (O)
NTS[a]	Hydrophobic	N.A.[c]	98 ± 2.0	111 ± 1	49 ± 1	N.A.
GTS[b]	Superhydrophobic	0	157.1 ± 3.8	167.3 ± 1.5	157.7± 2.2	N.A.
SLIPS1	Slippery	1.9 ± 0.2	110.9 ± 1.3	N.A.	N.A.	3.4 ± 0.2
SLIPS2	Slippery	3.0 ± 0.2	101.5 ± 1.2	N.A	N.A.	0.5 ±0.2
SLIPS3	Slippery	8.7 ± 0.2	93.6 ± 0.8	N.A	N.A.	0.2 ± 0.2
SLIPS4	Slippery	13.8 ± 0.2	88.2 ± 0.4	N.A	N.A.	0.2 ± 0.2
SLIPS5	Slippery	18.0 ± 0.2	84.1 ± 1.9	N.A	N.A.	0.2 ± 0.2

[a] ZnO/Al substrate with no treatment, [b] GLACO nanoparticle deposited surface, [c] not applicable.

On the SLIPS, a contact angle could not be measured using the above method as there was no direct droplet contact with the solid surface, only an observable liquid-liquid contact between droplet and lubricant. This liquid-liquid contact resulted in a lubricant wetting ridge surrounding the droplet base (see Figure 1(b)). Therefore, an apparent static contact angle, θ_{app}, was measured from the top of the wetting ridge [54]. Moreover, it was impossible to determine advancing or receding apparent contact angles by inflation/deflation experiments as the contact line was highly mobile. Therefore, DI water droplets (2 µl) were placed on the surface, and the stage was tilted in a step of 0.1° increments until the droplet was observed to move smoothly across the surface. This gave the sliding angle, θ_{SA}, of the surface, which was the smallest angle at which drop movement

was observed. The water droplets' sliding angles and contact angles on both the treated and untreated surfaces are listed alongside the contact angles on these surfaces (see Table 1).

2.3. Droplet impact tests

Droplets of deionized water with an initial diameter, $D_d = 1.89 \times 10^{-3}\, m$, were generated from a hypodermic needle (BD Microlance, inner diameter $D_n = 1.5\, x\, 10^{-3}\, m$) mounted on a 2D positioner using a syringe pump. The droplets were released from a set height, $H = 0.1\, m$, with an initial velocity of zero to reach the desired velocity before the impact on the surface of the device (which was set horizontally). The capillary regimes investigated in this study were in a range that the maximum spreading diameter scales with $We^{0.25}$.[12] The impact sequences and their outcomes were captured from a side view using a high-speed camera (HotShot 1280 CC) with Navitar 6.0× zoom lens and 0.5× objective lens at 5000 frames per second and a resolution of 432 x 244 pixels. MATLAB image processing toolbox was used to analyze the temporal evolution of the droplet contact width. A set of systematic experiments was performed to fully understand the effect of SAW propagation on the SLIPS and superhydrophobic surfaces on droplet impact dynamics. The thickness of the lubricating layer and the power of the SAWs were varied in these experiments that were carried out under atmospheric conditions (temperature of 23 ± 0.5 °C and 30 ± 1 % relative humidity). Under these conditions, the deionized water's density and surface tension were 995 $kg \cdot m^{-3}$ and 0.072 $N \cdot m^{-1}$, respectively. Each test was repeated four times for a given SAW power and surface treatment to confirm the repeatability.

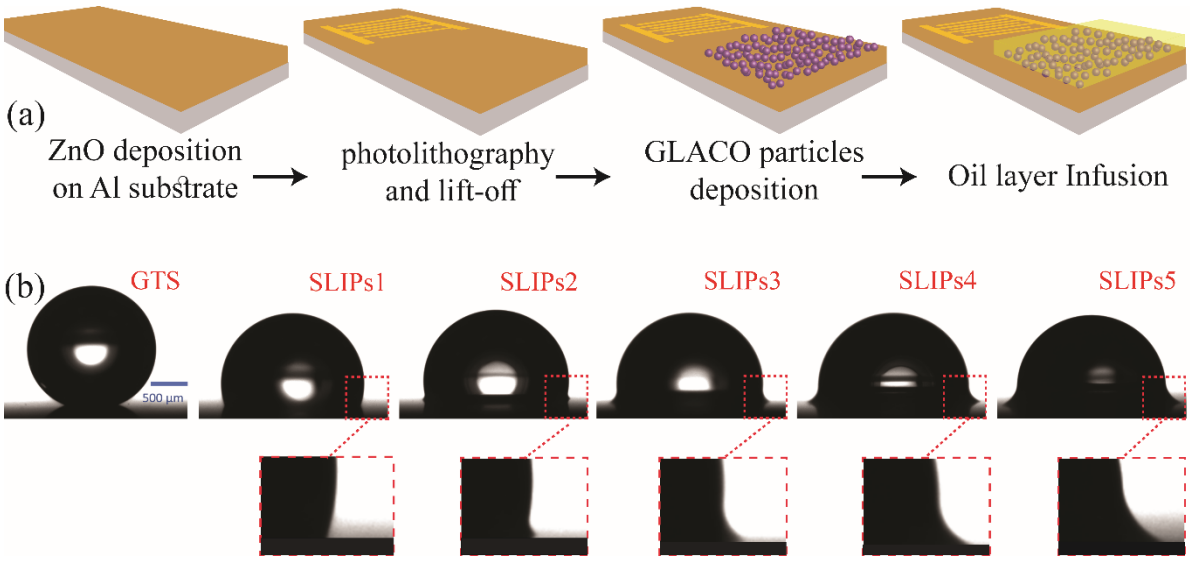

Figure 1: (a) A schematic illustration of SLIPS production. In all the experiments, the droplet impacts onto a region far from the SAW generation area (i.e., IDTs), (b) Droplet shape on different surface treatments. The embedded images show the corresponding wetting ridges on the different SLIP surfaces.

Results and discussion

3.1. Droplet impact dynamics without SAWs

The snapshots of droplet free impact (FI, i.e., no SAW applied) on the device's surface with different surface treatments are presented in Figure 2. After the impact, the liquid's initial kinetic energy is either dissipated or converted into surface energy [48]. Energy dissipation mainly happens due to the internal recirculations inside the liquid medium (viscous dissipation) or interaction of the liquid and solid (effect of friction and TPCL pinning) [48]. After reaching the maximum spreading radius, the stored surface energy starts to be converted into kinetic energy, and the droplet retracts towards the impact point. The determining factor of the impact outcome is the energy dissipation during the spreading phase [49]. The main sources of energy dissipation during

the impact are viscous dissipation (both lubricant and water) and the TPCL pinning, F_P, which can be expressed by [55]:

$$F_P = \frac{24}{\pi^3}\gamma_{lv} w\{cos(\theta_{rec}) - cos\ (\theta_{adv})\} \quad (1)$$

where γ_{lv} is the droplet liquid surface tension, w is the contact width, and θ_{rec} and θ_{adv} are the receding and advancing contact angles, respectively.

Figure 2(a) illustrates the droplet impact on the ZnO/Al device's surface without surface treatment (e.g., non-treated surface, NTS). Due to the high surface roughness of the substrate and a large contact angle hysteresis, the pinning force causes significant dissipation of the droplet's initial kinetic energy, and the droplet adheres to the surface at the end of the retraction phase.

The temporal evolution of the droplet impact on the superhydrophobic surface (e.g., GLACO-treated surface, GTS) is illustrated in Figure 2(b). During the impact of the drop onto this superhydrophobic surface, an air cushion usually is present within the nanostructures [56]. The trapped air results in a short and discrete TPCL that significantly reduces the liquid adhesion on the solid surface [57]. Therefore, the energy dissipation is reduced, and the droplet has enough kinetic energy to be separated from the surface at the end of the retraction phase as a liquid jet.

Droplet free impact phenomena on SLIPS1 (e.g., conformal SLIPS with a minimum lubricant layer thickness in this study) are shown in Figure 2(c). The presence of a lubricant film between the solid surface and the water droplet inhibits a direct water-solid contact, and therefore significantly reduces energy dissipation due to contact line pinning (evident from the sliding angle data in Table 1). As the energy dissipation due to the contact line pinning is significantly reduced (compared to the droplet impact on the NTS), more energy is available to promote a partial rebound from the surface in the retraction phase. However, the SLIPS causes higher adhesion to droplets in the direction normal to the surface [58]. Therefore, only a partial droplet rebound is observed.

Figure 2(c) clearly shows that for the SLIPS, a capillary neck forms and breaks, leaving behind a smaller droplet on the surface, whereas on the surface of GTS, it appears to be a full rebound.

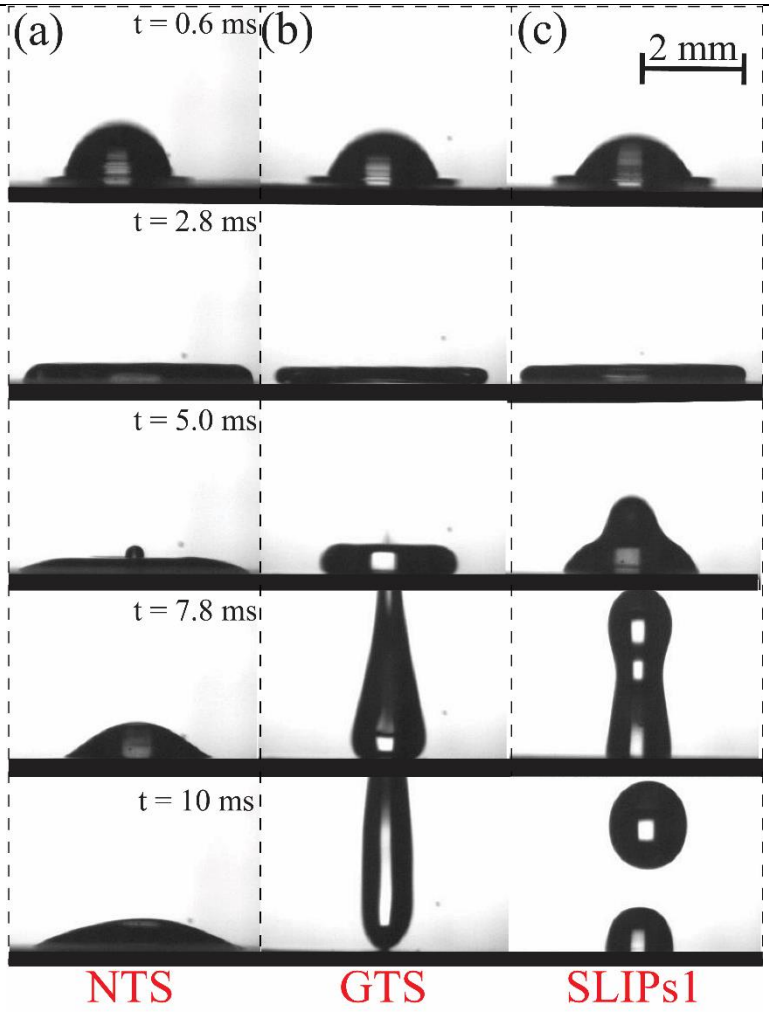

Figure 2: Snapshots of water droplet free impact on the solid surface of ZnO/Al SAW device with (a) no treatment, (b) superhydrophobic surface, (c) SLIPS with lubricant thickness of 2 µm, surface treatment. In all experiments, a droplet with a volume of 3.56 µl is impacting the solid surface with a velocity of 1.4 m/s. All the impacts on the surfaces are recorded at frame rate of 5000 fps. For comparisons between the impact dynamics all the snapshots on all three surfaces are illustrated at the same time.

3.2. Droplet impact dynamics with SAWs

Figure 3 shows the recorded droplet impact images onto different substrates while SAWs propagate on the solid surface. The SAWs are generated ~2 sec before the droplet impact (to avoid potential heating effect) by applying an RF power of 20 W to the IDTs. Our observations showed that the applied SAW energy did not apparently change the impact regime after droplet impact on the untreated surface of ZnO/Al SAW device. The droplet was still retained by the surface without any rebounding (see Figure 3(a)). However, the droplet was slightly transported along the SAW propagating path, while significant vibrations and interface deformations were noticed during the impact. With the SAW power increased from 5 W to 35 W, droplet rebound was not observed in all the impact experiments.

Interestingly, for the porous and superhydrophobic (GTS) surface, no apparent differences were observed in the droplet impact dynamics with and without applying SAW power (compare Figures 2(b) and 3(b)). For a preliminary interpretation, we consider an equivalent acoustic impedance model for acoustic transmission from the substrate through a porous layer filled with either air or oil to explain the basic features of the observation. Using the Johnson-Champoux-Allard (JCA) equivalent fluid model, the acoustic impedance Z_p of the porous layer can be obtained by [59]:

$$Z_P = \sqrt{\rho_{eff} K_{eff}} \tag{2}$$

where,

$$\rho_{eff} = \alpha_\infty \rho_0 \left(1 + \frac{\sigma \phi}{j\omega \rho_0 \alpha_\infty} \sqrt{1 + j\omega \frac{4\alpha_\infty^2 \eta \rho_0}{\sigma^2 \Lambda^2 \phi^2}} \right) \tag{3}$$

$$K_{eff} = \frac{\gamma_0 P_0}{\left[\gamma_0 - (\gamma_0 - 1) \left(1 + \frac{8\eta}{j\omega Pr \rho_0 \Lambda'^2} \sqrt{1 + j\omega \frac{Pr \rho_0 \Lambda'^2}{16\eta}} \right)^{-1} \right]} \tag{4}$$

where α_∞ is the tortuosity and ϕ is the porosity of the nanoporous layer, ρ_0 and η are the density and viscosity of the fluid in the porous layer, $\omega = 2\pi f$ is the angular frequency of the wave, σ is the flow resistivity of the porous layer, η is the dynamic viscosity of the fluid, $\Lambda = \sqrt{8\alpha_\infty k_0/\phi}$ is the viscous characteristic length [60] and $\Lambda' = 3.33\sqrt{8\alpha_\infty k_0/\phi}$ is the thermal characteristic length of the porous layer [61] $k_0 = \eta/\sigma$, γ_0 is the ratio of specific heats, P_0 is the static pressure and Pr is the Prandtl number. The porosity is taken as 0.26 assuming a hexagonal closed packing of nanoparticles comprising the porous layer. The tortuosity is estimated using the model for spherical particles by Lanfrey et al [62]:

$$\alpha_\infty = \phi/[1-(1-\phi)^{\frac{2}{3}}] \tag{5}$$

The flow resistivity ($\sigma = 8\eta/\phi r^2$) is obtained via Darcy's law assuming a Poiseuille flow and that the porous layer is equivalent to an array of capillary tubes with a radius equal to the pore size (r).

The equivalent acoustic impedance (Z_{eq}) of the porous layer and water droplet, as seen by a wave travelling in the substrate, can be obtained from [63]:

$$Z_{eq} = Z_P \frac{Z_w + jZ_P\, tan(k_P t_P)}{Z_P + jZ_w\, tan(k_P t_P)} \tag{6}$$

where $Z_w = \rho_w c_w$ is the acoustic impedance of water, ρ_w is the density of water, and c_w is the speed of sound in water. t_P is the thickness of the porous layer and $k_p = \omega\sqrt{\frac{\rho_{eff}}{K_{eff}}}$ [59]. The nanoporous layer on our substrates has a thickness of ~1 μm. For the superhydrophobic surface, Z_{eq} is obtained as 1.04×10^4 rayl, which is almost three orders smaller than the acoustic impedance of the substrate ($Z_{substrate} = 1.7 \times 10^7$ rayl). The reflection coefficient $|(Z_{eq} - Z_{substrate})/(Z_{eq} + Z_{substrate})|^2$ for this case is obtained as 0.998. Therefore, a large

impedance mismatch indicates weak transmitted acoustic energy from the substrate to the air-water films.

This simple model can explain key features of our observation that there is no apparent change of the drop impact dynamics on the GTS surface. These results are also interesting since previously, Sudeepthi et al. reported a Cassie–Wenzel wetting transition on a superhydrophobic nanoparticle surface induced by SAWs [64]. Their results showed that by subjecting the superhydrophobic nanoparticle surface to SAWs constantly for ~ 20 s, the liquid could penetrate the nanoparticles, and the wetting behavior of the surface can irreversibly be changed to a Wenzel state. However, for the impact cases in this study, due to the fast dynamics of the phenomenon (duration of the whole impingement is ~8 ms), the liquid (water) does not have enough time to penetrate the porous nanoparticulate structures. Therefore, due to the existence of air gaps, the surface vibration will not be effectively transmitted into the liquid medium, and thus the impact dynamics will not be changed.

In order to confirm this, we have done verification using droplet transportation on the superhydrophobic (e.g., GTS) surface. We located a droplet with the same volume on the surface and applied SAWs with various applied power to the IDTs. We did not observe any pumping or jetting behavior after applying a high power (34 W) to the SAW device, proving wave energy has not been effectively transferred from the top surface into the droplet.

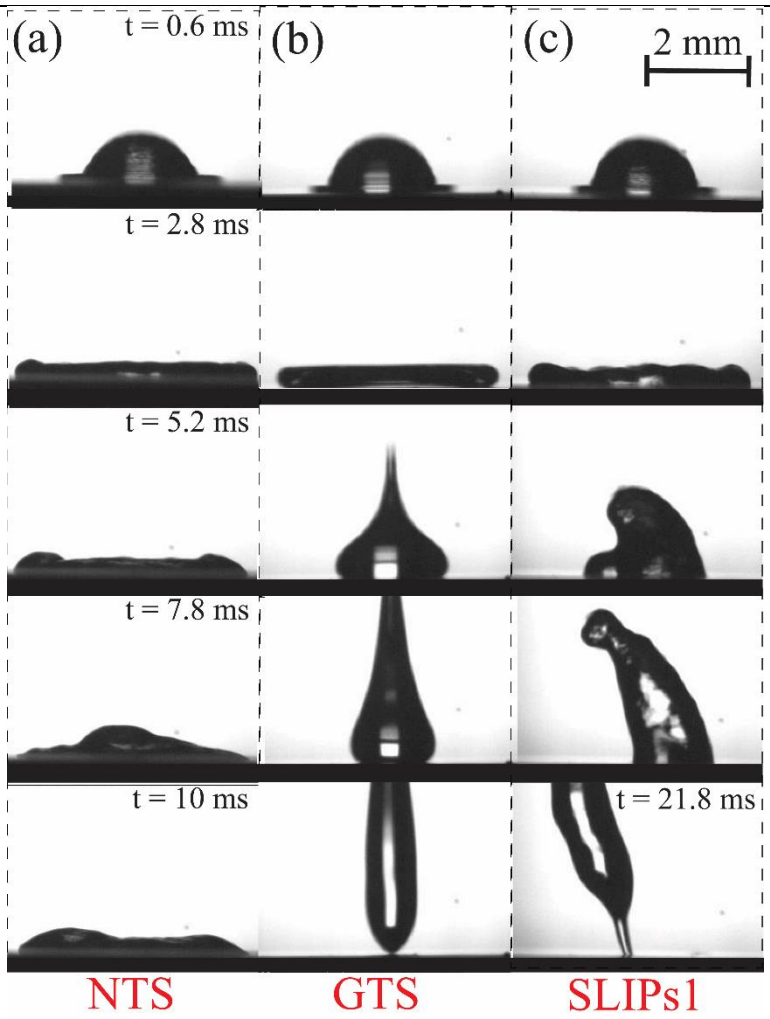

Figure 3: Snapshots of water droplet impact on the solid surface of ZnO/Al SAW device with (a) no treatment (NTS), (b) superhydrophobic and porous surface (GTS), (c) SLIPS with lubricant thickness of 2 µm. In all the experiments, a droplet with a volume of 3.56 µl is impacting the solid surface with a velocity of 1.4 m/s. During the impact, SAW with the power of 8.5 dB (~20 W) is propagating from right to left. All the impacts on the surfaces were recorded at a frame rate of 5000 fps. The first four rows compare the droplet shapes at the same time after the onset of the impact. The last row shows the droplet shapes after 10 ms for the NTS and at the separation moment for the GTS and SLIPS1.

Figure 3(c) shows that after the lubricant has been infused into the superhydrophobic layer (in which a conformal SLIPS is formed and the air gaps in the porous medium are filled), the SAW energy can be effectively transmitted to the droplet during the impact. If we use equations (1) and (2) for an oil film (and $K_{eff} = 1.02 \times 10^9$ for the oil), we can obtain that the acoustic impedance characteristics of the SLIPS is 3.6×10^7 and the reflection coefficient is 0.277. The reduced value of the reflection coefficient indicates a significantly larger SAW energy being transferred from the substrate as compared to the case of the porous and superhydrophobic (e.g., GTS) coating. For the SLIPS with a thin lubricant layer of 2 μm (see Figure 3(c)), the impact regime is changed from the partial rebound to the full jetting. The last snapshot of Figure 3(c) shows that the SAW also modifies the rebounding angle.

To quantitatively compare the effect of SAW on droplet impact dynamics, we investigated the temporal evolution of the normalized contact width, β (i.e., the ratio of the droplet contact width to the droplet's initial diameter). These data were obtained from the image processing of the videos taken from the experiments' side views. As shown in Figure 4(a) for the NTS case, no remarkable difference is observed by applying the SAW power. For the droplet impact on the NTS (See Figure 4(a)), the experimental results revealed that the SAW energy during the impact is not large enough to overcome the adhesion forces during the impingement, and therefore by applying a SAW power up to 15 W, the droplet could not be separated from the surface. Thus, after the contact width is reduced (during the retraction phase) by ~30%, it starts to increase (due to gravitational and surface energy), and then the droplet adheres on the surface. However, since the external SAW energy is applied to the system during the impact, the droplet is transported on the surface by applying the SAW. For both cases, the final contact width is similar. A comparison between the droplet's normalized contact width in the impact scenarios on the surface with superhydrophobic (GTS)

treatment (see Figure 4(b)) shows that impact dynamics remain unchanged by applying the SAWs. In these scenarios, SAW energy has not been effectively transmitted to the impacting droplet, as explained before.

The lubricant penetration within the air gaps leads to the transmission of SAW energy into the droplet during the impact, thus changing the droplet's impact dynamics. As illustrated in Figure 4(c), for the droplet impact on the SLIPS with a lubricant thickness of 2 μm, SAWs change the impact regime from a partial rebound to a complete rebound, and the droplet is fully separated from the surface within ~22 ms.

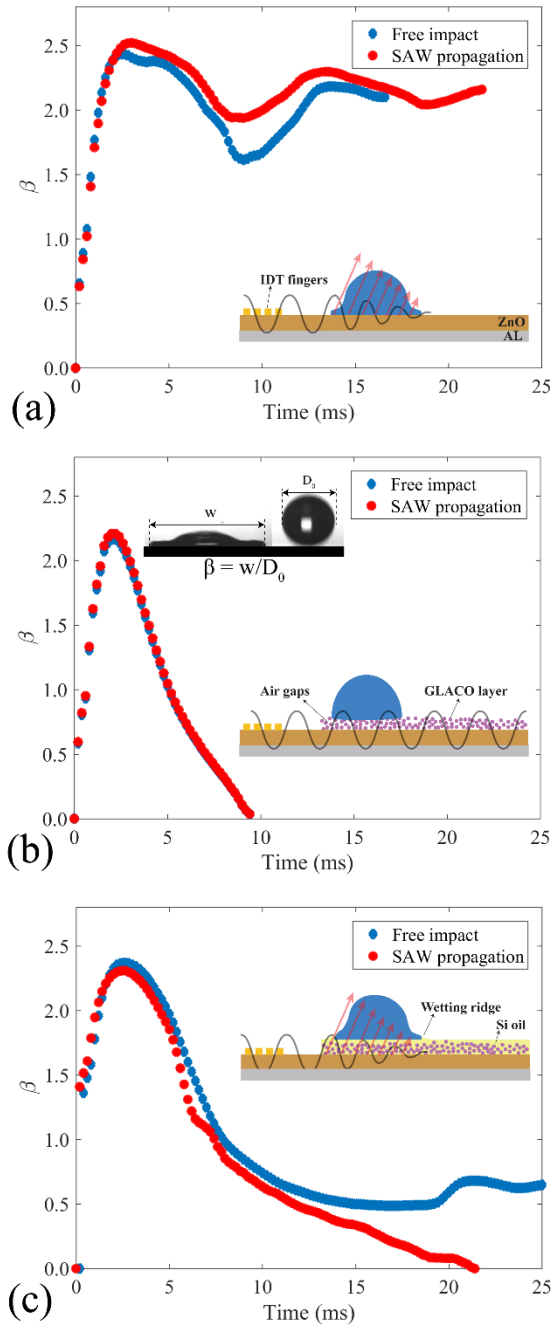

Figure 4: Temporal evolution of the normalized contact width for droplet impact on (a) surface without treatment (e.g., NTS), (b) Surface covered with superhydrophobic nanoparticles (e.g., GTS), and (c) conformal SLIPS (SLIPS1). For all the experiments, a

droplet with a volume of 3.56 µl is impacting onto the solid surface with a velocity of 1.4 m/s. SAW with a power of 20 W is propagating on the surfaces.

To better understand SAWs' effect on impact dynamics, we analyze the velocity of the droplet edges, and the obtained results are shown in Figure 5. The blue lines show the edge velocities for the FI scenarios, and the red lines illustrate SAW scenarios' velocities. The spreading phase is between the impact moment and when left edge velocity (LEV) and right edge velocity (REV) are reduced to zero in all the figures. After that period, the retracting phase is started while the magnitudes of REV and LEV start to increase (for a better illustration, these two areas are separated by the shaded areas as shown in Figure 5(b)). For all the cases, the LEV and REV have their maximum values just after the impact, but they decrease sharply as the droplet spreads on the surface.

We have shown in our previous studies that 75% to 90% of the droplet's initial kinetic energy is dissipated during the spreading phase due to the viscous dissipation (which is a result of internal recirculation inside the droplet) [48] and the work done by the resistive forces at the three-phase contact line area ($W_R \propto \frac{cos(\theta_{rec}) - cos(\theta_{adv})}{1-cos(\theta_{adv})}$) [49]. From the literature, we also know that the retraction velocity scales as $\sqrt{1 - cos\ (\theta_{rec})}$ [65]. Therefore, at the end of the retract phase, the droplet cannot rebound from the NTS surface due to higher energy dissipation by the resistive forces and lower retracting velocity. By applying SAWs on the surface during the impact, a pressure field is applied to the liquid medium along the Rayleigh angle ($\theta_R = sin^{-1}\frac{v_L}{v_S}$, where v_L and v_S are the sound velocity in the liquid and solid mediums). The applied SAW energy to the droplet can be evaluated by [64]:

$$E_{SAW} \sim \frac{1}{2}\rho V(A\omega)^2 \qquad (7)$$

where V is the droplet volume, ω and A are the resonant frequency and amplitude of SAWs, and ρ is liquid density. To estimate the SAW amplitude, the empirical correlation $\frac{A}{\lambda} = 8.15 \times 10^{-6} {P_{RF}}^{0.225} + 5 \times 10^{-6} {P_{RF}}^{0.8}$ was used, where λ is the SAW wavelength, and P_{RF} is the applied power to the IDTs in Watts [66].

By applying SAWs to a droplet impacting on NTS, the LEV is similar to free impact scenarios. However, due to the transferred SAW energy on the right edge, the SAWs resist the droplet's spreading, and thus a REV is reduced (compared to that in the free impact scenario). Once the droplet starts to retract, since the X-component of SAW force and contact line motion directions are aligned, the REV is increased up to 0.17 m/s and then decreased to zero.

The temporal evolutions of REV and LEV values for the droplet impact on the superhydrophobic (e.g., GTS) surface are illustrated in Figure 5(b). As shown in Figure 5(b), both the velocities are similar to those of the NTS impact scenario during the spreading. During the spreading phase, the primary energy dissipation mechanism is viscous dissipation (e.g., due to the internal recirculation). The differences in the surface treatment do not show an effect on the velocities. However, since the difference between the advancing and receding contact angles for the GTS is low, the energy dissipation due to the resistive force is insignificant compared to that in the NTS case. Once the retraction phase starts, both the edges' velocities increase sharply (see Figure 5(b)) to a peak value and then slightly decrease until the droplet is separated from the surface after 9.4 ms as a jet.

The REV and LEV dynamics are pretty different for the impact cases on SLIPS since there is a liquid layer between the droplet and the solid surface. Figure 1(b) shows that a wetting ridge is formed during the droplet’s impact onto the SLIPS, which dissipates the droplet kinetic energy.

Figure 5(c) shows that the maximum spreading velocity for the impacts is up to 50% lower than those on the superhydrophobic nanoparticle surface (where the resistive force against the contact line motion is negligible). The formation of the wetting ridge around the droplet rim during the spreading phase resists the motion of the three-phase contact line. For the conformal SLIPS scenario, after reaching the maximum spreading radius (i.e., both REV and LEV become zero), the TPCL starts to retract toward the center with an increasing velocity. After reaching a peak value (for both the REV and LEV), the contact line velocity gradually decreases until a sub-unit is separated from the main droplet, and then the contact line velocity becomes zero. During the retraction phase, the contact line acceleration (i.e., the gradient of the REV and LEV lines) is higher for the GTS impact case than the conformal SLIPS case. This can be explained by comparing the resistive forces in the contact line regions for the GTS and SLIPS impact scenarios. As discussed above, there is no significant resistive force against the contact line motion in the GTS impact (since the contact angle hysteresis is quite small), the formed wetting ridge around the droplet resists the contact line motion for the SLIPS cases. By applying SAWs from the right edge, initially, a decrease of REV up to 50% can be observed. More interestingly, REV becomes zero at a time of 1.6 ms sooner than LEV, meaning that the retract phase in the right side of the droplet (induced by SAWs) starts while the left edge is still spreading. After reaching their peak values, both the REV and LEV are reduced to ~0.09 m/s and then the droplet is detached from the surface. The X-component of the SAW force transports the droplet horizontally across the device surface during its impingement.

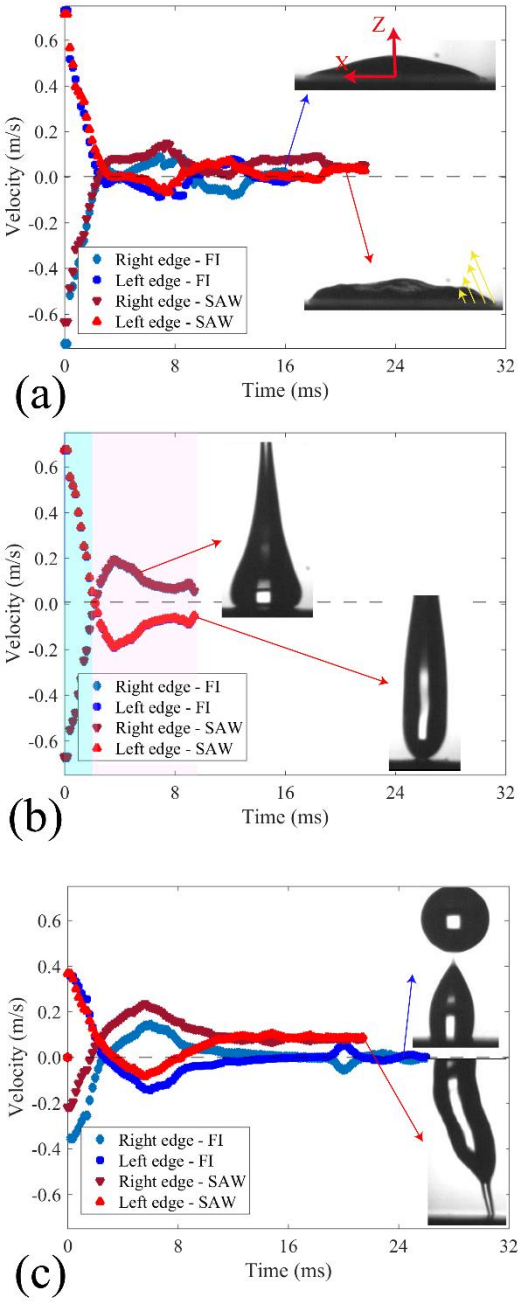

Figure 5: The velocities of right and left edges of the droplet during the impact along X-direction for droplet impact on the solid surface of ZnO/Al SAW device with (a) non-treated surface (NTS), (b) surface covered with GLACO nanoparticles (GTS), and (c) conformal SLIPS (SLIPS1). In all the experiments, a droplet with a volume of 3.56 µl is impacting the

solid surface with a velocity of 1.4 m/s. For the cases with SAW propagation (i.e., red markers), the power of the wave is 20 W, and it is propagating in X-direction (i.e., right to the left)

3.3. Effect of lubricant thickness on impact dynamics

We further carried out droplet impact experiments on SLIPS with various lubricant thicknesses, and the results are shown in Figure 6(a). In all the experiments, a droplet with a volume of 3.56 µl and an impact velocity of 1.4 m/s was impacted onto the surface. For the free impact scenarios, a partial rebound impact regime was observed for the droplet impacting the SLIPS1 (conformal) surface. By increasing the lubricant thickness to 3 µm, the impact regime was changed from a partial rebound to complete detachment, and the droplet was separated from the surface after 22.6 ms (see Figure 6(a)). For the surfaces with an oil layer thickness of 8.7 µm, the CT was ~21.6 ms. However, this value did not change significantly with the further increase of lubricant thickness, as shown in Figure 6(a).

To explain this phenomenon, we can focus on the energy evolution during the droplet's impact on different surfaces. Assuming that the droplet has initial energy of E_0, which is the sum of initial kinetic energy and surface energy of the droplet. Our previous numerical results have shown that the gravitational energy conversions can be negligible during the droplet's impact [48]. During the droplet's spreading, the initial kinetic energy of the droplet starts to dissipate or is converted into surface energy [48]. The main mechanisms for energy dissipation are (1) viscous dissipation (i.e., the irreversible process which converts the work done by shear stresses of adjacent layers of fluid to heat); and (2) strong interaction between the water and oil at their interface (such as adhesion force in the oil-water interface and resistance of wetting ridge against three-phase contact line motion).

With the increase of the oil thickness, the balance between the energy dissipation and surface energy has been changed mainly due to two reasons.

Firstly, as the oil thickness increases, the wetting ridge's height increases, as shown in Figure 1(b). Therefore, the wetting ridge could prevent the contact line motion during the droplet's spreading and retract phases, and thus more energy is dissipated during the impact.

Secondly, during the droplet's impact onto SLIPS, the deformation of oil-water interface during the droplet's spreading phase could store more energy. As illustrated in Figure 6(b), the total interfacial/surface energy of an oil-liquid-air system ($E_{Surface}$) for a droplet in contact with the oil layer of SLIPS can be given by:

$$E_{Surface} = \gamma_{LA} S_{a,0} + \gamma_{LO} S_{o,0} + \gamma_{OA} S_{\infty} \quad (8)$$

where γ_{LA}, γ_{LO} and γ_{OA} are the interfacial tensions (i.e., surface energies per unit area) of the droplet-liquid-air (72.8 mN/m), droplet-liquid-oil (38 mN/m), and oil-air (19.8 mN/m) interfaces, respectively. $S_{a,0}$ and $S_{o,0}$ are the areas of the droplet interfaces in contact with air and oil, and S_{∞} is the area of the oil layer surface in contact with the ambient air. Here, we define the changes of surface energy associated with droplet spreading as $E_S = E_{surface} - \gamma_{OA} S_{\infty}$. The reference surface energy, $E_{S,0}$, is equal to the droplet surface energy at the onset of impact [49]. The amount of the additional surface energy (which is converted from the initial kinetic energy during the spreading) at the maximum spreading moment, $E_{S,m}$ is:

$$E_{S,m} = \gamma_{LA}(S_{a,m} - S_{a,0}) + \gamma_{LO}(S_{o,m} - S_{o,0}) \quad (9)$$

where $S_{a,m}$ and $S_{o,m}$ are the areas of the droplet interfaces in contact with air and oil at the maximum spreading moment.

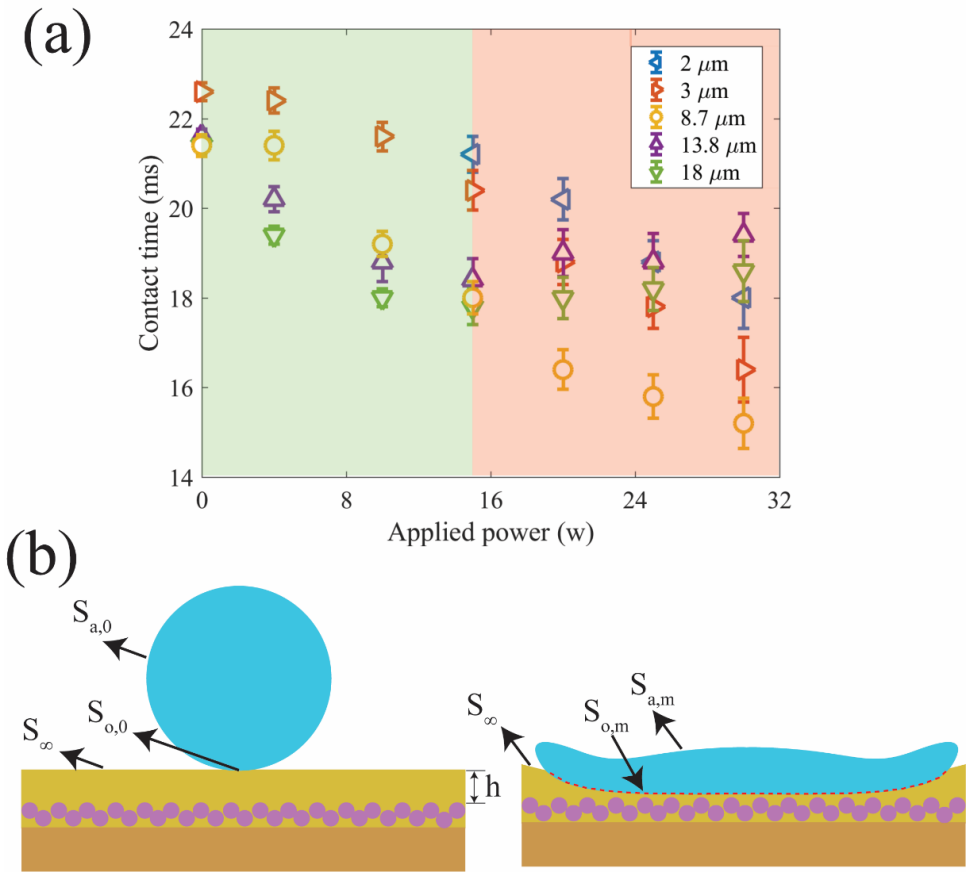

Figure 6: (a) Effects of applied SAW power and lubricant thickness on droplet contact time. In all the experiments, a droplet with a volume of 3.56 µl and a velocity of 1.4 m/s impacts onto SLIPS surfaces with various oil thicknesses. (b) A schematic illustration of droplet interface deformations during the spreading phase. The dashed line in the right image illustrates the oil-water interface. S_a and S_o are the areas of the droplet interfaces in contact with air and oil, and S_∞ is the area of the oil layer surface in contact with the ambient air. Additionally, subscripts 0 and m refer to the onset of impact and maximum spreading moment, respectively.

For the conformal SLIPS, since the volume of the oil layer on top of the GLACO coating is negligible, the second term in Eq. 9 becomes zero, and thus, there could be less kinetic energy provided during the droplet's retract phase, which will not easily achieve a complete rebound. For the SLIPS with a thicker oil layer, the value of h (see Figure 6(b)) is larger, and the oil medium could have more space to deform. Thus, the value of $S_{o,m}$ is increased, and more energy could be stored as the surface energy during the spreading phase. This additional surface energy could be converted back to kinetic energy during the retract phase, thus providing the droplet with more energy to be detached from the surface in a much shorter time. For example, by increasing the thickness of the oil layer to 3 μm, the stored surface energy during the spreading phase is increased. Besides, due to the formation of a larger wetting ridge, much more energy is dissipated; therefore, a complete rebound was observed at 22.6 ms. By further increasing the oil layer thickness to 8.7 μm, the additional surface energy overcomes the dissipated energy due to wetting ridge resistance to the contact line motion.

By applying SAWs to the SLIPS during the impingement process, the balance between the energy terms has been significantly changed. The applied SAW energy increases the kinetic energy of the droplet during the impact. Although the internal recirculation inside the droplet could partially dissipate the droplet's kinetic energy, the rest of the applied SAW energy can still be converted into kinetic energy. This additional kinetic energy will reduce the contact time and change the direction of the rebouncing droplet. As clearly shown in Figure 6(a), by applying the SAWs to SLIPS samples, the contact times are decreased compared to those for the free impact scenarios. For instance, a maximum of ~30% reduction in the contact time was observed by applying SAW with a power of 30 W to the SLIPS3 during the impact. By analyzing the data, Figure 6(a) could be divided into two regions for discussions: (a) a lower SAW power region (i.e., with the applied

SAW power lower than 15 W); and (b) a higher SAW power region (i.e., with the applied SAW power higher than 15 W). At the lower SAW power region (e.g., the green shaded area in Figure 6(a)), the contact time decreases by increasing both the oil thickness and the applied SAW power. As explained already, by increasing the oil layer thickness, the surface energy stored in the oil medium could enhance the droplet's rebounding. Additionally, by increasing the applied SAW power, more kinetic energy is transferred from the SLIPS to the droplet during its impingement process, which accelerates the droplet's detachment from the surface. However, in the higher SAW power region (see the right-hand shaded area in Figure 6(a)), the minimum contact time is achieved with an oil layer thickness of 8.7 μm (SLIPS3), whereas further increase of oil layer thickness results in the increase of the contact time.

We repeated the experiments for droplet impacts on samples of SLIPS3, SLIPS4, and SLIPS5. In these experiments, the camera was adjusted to locate at ~10 cm above the surface with an inclination angle of 15^{o}, in order to observe the surface of the samples during the impact. We found that at higher SAW powers (i.e., larger than 15 W), the oil layer was apparently moved forward by applying SAWs on the samples of SLIPS4 and SLIPS5 (see the supplementary video 1), but not on SLIPS3. These results clearly prove that by applying higher SAW powers, part of the SAW energy has been used to drive the oil layer on the surface for the thicker oil layer samples of SLIPS4 and SLIPS5. Therefore, less powers could be available to effectively retract/detach the droplet from the surface during the impact.

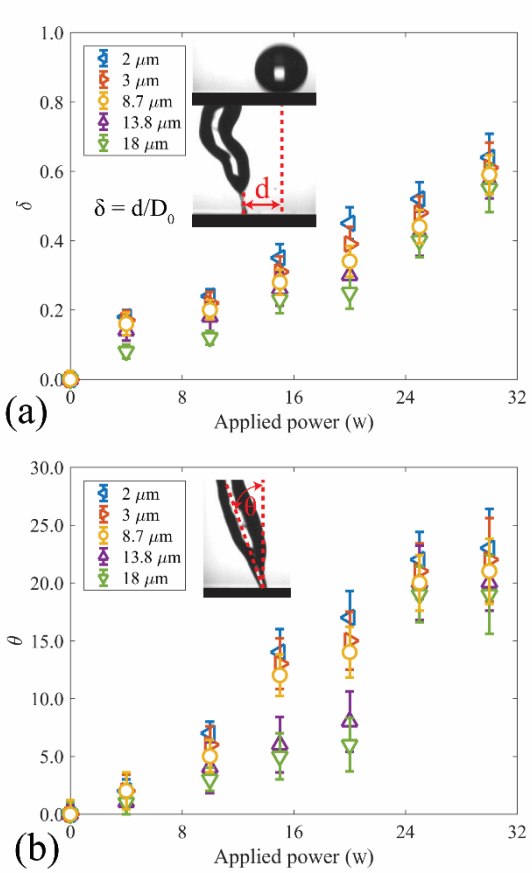

Figure 7: (a) Droplet's horizontal transportation distances and (b) droplet rebounding angles along the solid surface during the impact normalized by initial droplet diameter. In all experiments, a droplet with a volume of 3.56 µl is impacting the solid surface with a velocity of 1.4 m/s.

To explore SAWs' potential to control the droplet impact behaviors on SLIPS, we studied other impact parameters such as the droplet's horizontal transportation distances on the surface before the liquid jet's detachment and redirection. The horizontal movement of the droplet during the impingement, δ ($\delta = d/D_0$, where d is the distance between the impact and detachment points, and D_0 is the original droplet diameter) as a function of the applied SAW power is illustrated in Figure 7(a). Our results indicate that by decreasing the lubricant thickness or increasing the applied SAW power, the horizontal movement of the droplet has been increased. In the literature, it is well

explained that SAWs are attenuated due to the generation of acoustic streaming when the SAW energy is dissipated into a liquid medium such as silicone oil [67]. With the increase of oil layer thickness, the wetting ridge of droplet is enlarged (see Figure 1(b)), and thus the resistance against the droplet motion is increased. Partial of the SAW energy has also been dissipated into the oil layer. These two factors lead to the decrease of value δ. By increasing the SAW power or wave amplitude, more momentum along the SAW propagation direction is applied to the droplet, and thus the value of δ is increased. The direction angles of the liquid jet during the retraction phase induced by the SAWs are illustrated in Figure 7(b). The direction angle was measured as the deviation from the vertical direction in the anticlockwise direction (see the embedded figure for the definition). From Figure 7(b), we can see that this angle gradually increases due to the SAW actuation with a successive increase in the applied SAW power.

3.4. Effect of impact velocity on impact dynamics

We further performed three characteristic experiments of droplet impact with various impact velocities onto the conformal SLIPS. Three impact scenarios with the initial impact velocities of 1.0 m/s, 1.4 m/s, and 2.0 m/s were selected to investigate the effect of initial impact velocity on the impact dynamics. Figure 8(a) shows the obtained contact times as a function of the applied SAW powers. For the impact velocities of 1.0 m/s and 1.4 m/s, when the SAW power is lower than 15 W, the droplet cannot be detached from the surface at the end of the retract phase. For these two cases, the sum of kinetic energy and applied SAW energy at the end of the retract phase is not high enough to separate the droplet from the surface. Whereas when the applied SAW power is higher than 15 W, a complete rebound could be observed.

For the cases with the impact velocity of 2.0 m/s, droplets are fully separated from the surface at all the applied SAW powers (even in free impact cases), and the contact time is reduced by

increasing the impact velocity at higher powers (see Figure 8(a)). To explain this, we will consider the maximum spreading ratio of the droplet, β_{Max}. As illustrated in Figure 8(b), the maximum spreading ratio decreases by increasing the applied SAW power. We have observed similar behavior for the droplet impact onto a hydrophobic surface and have explained (with numerical simulation results) this phenomenon in our previous publication [49]. We further explain why the contact time is shorter for the cases with higher impact velocities at the same applied SAW power based on the maximum spreading radius of the droplet. The amount of the SAW energy transferred to the droplet is a function of the droplet contact area with the surface. By increasing the initial impact velocity, the maximum spreading radius of the droplet increases (see Figure 8(b)), and thus more energy is transferred to the droplet during the impingement. This increased transferred energy, which in turn reduces the droplet contact time.

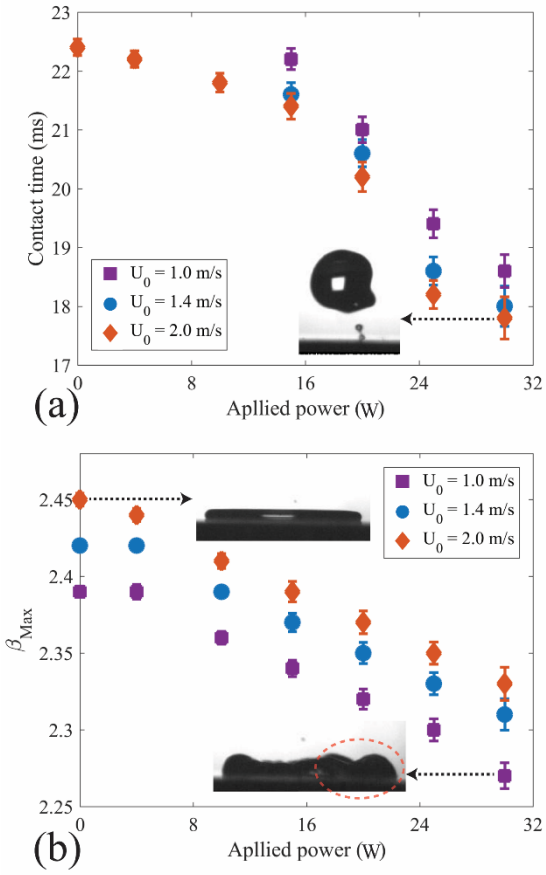

Figure 8: (a) Droplet contact time as a function of applied SAW power for different initial impact velocities. (b) Maximum spreading ratio β_{Max}as a function of applied SAW power for different initial impact velocities. In all experiments, a droplet with a volume of 3.56 µl is impacting onto the SLIPS1.

For many industrial applications, including aviation, transportation, wind turbines, and telecommunications, it is desirable to avoid condensation or ice formation on surfaces [65]. Anti-sticking or anti-icing surfaces have been designed to achieve this goal. Typically, these surfaces are designed for scenarios when a supercooled droplet impacts onto a surface, which could be at a sub-zero temperature. The contact time between the liquid and solid surface must be lower than the ice nucleation time to prevent ice formation. Therefore, anti-icing surfaces should have the

minimum possible contact time with the impact droplets. Besides, it is crucial to avoid droplet deposition on a surface for many industrial applications, and it is ideal for removing the droplet from the impact area in the shortest possible time to keep the surface uncontaminated. Overall, our results showed that integration of SLIPS and thin-film SAW technologies could lead to the design of a smart surface that can reduce contact time and change the impact regime. Besides, the rebounding angle can also be actively altered, which might be attractive for 3D-bioprinting applications.

Conclusion

This paper introduced a methodology to control the droplet impact on surfaces using ZnO/Al SAW devices, which were coated with various surface treatments, namely GLACO nanoparticles and SLIPS. Our results showed that when the surface was coated with nanoparticles forming a superhydrophobic layer, SAWs did not alter the droplet impact dynamics due to a large acoustic mismatch between the device's surface and this nanoporous superhydrophobic layer. However, when a lubricant layer was infused into the nanopores among the nanoparticles, SAWs can be transmitted from the device's surface through the liquid medium during the droplet impact, thus changing the impact regime, contact time, and rebounding angle. The results showed that the presence of SAWs during the droplet impact on SLIPS can significantly change the contact time and rebounding angle. We further investigated the effect of the oil thickness and SAW power on the impact dynamics, and the contact time was reduced up to 30% by applying SAWs with an optimum oil lubricant thickness of ~8 μm. Our work offers an effective way to use SAWs with SLIPS to reduce the contact time and alter the droplet rebound angles.

AUTHOR INFORMATION

Author ORCIDs:

Mehdi H Biroun: https://orcid.org/0000-0003-3269-7749

Luke Haworth: https://orcid.org/0000-0003-1411-3199

Prashant Agrawal: https://orcid.org/0000-0002-6558-2684

Bethany Orme: https://orcid.org/0000-0003-4280-7702

Glen McHale: https://orcid.org/0000-0002-8519-7986

Hamdi Torun: https://orcid.org/0000-0002-7882-286X

Mohammad Rahmati: https://orcid.org/0000-0003-4903- 5370

YongQing Fu: https://orcid.org/0000-0001-9797-4036

Corresponding Author

* Prof. Richard Yongqing Fu, email: richard.fu@northumbria.ac.uk

Acknowledgments:

This work was financially supported by the UK Engineering, and Physical Sciences Research Council (EPSRC) grants EP/P018998/1, EPSRC NetworkPlus in Digitalised Surface Manufacturing EP/S036180/1, and Special Interests Group of Acoustofluidics under the EPSRC-funded UK Fluidic Network (EP/N032861/1). We also appreciate the support from EPSRC Centre for Doctoral Training in Renewable Energy Northeast Universities (ReNU) for funding through grant EP/S023836/1.

References

(1) Cionti, C.; Taroni, T.; Meroni, D. Bouncing Droplets: A Hands-On Activity to Demonstrate the Properties and Applications of Superhydrophobic Surface Coatings. *J. Chem. Educ.* **2019**. https://doi.org/10.1021/acs.jchemed.9b00406.

(2) Yonemoto, Y.; Kunugi, T. Analytical Consideration of Liquid Droplet Impingement on Solid Surfaces. *Sci. Rep.* **2017**, *7* (1). https://doi.org/10.1038/s41598-017-02450-4.

(3) Breitenbach, J.; Roisman, I. V.; Tropea, C. From Drop Impact Physics to Spray Cooling Models: A Critical Review. *Exp. Fluids* **2018**, *59* (3), 55. https://doi.org/10.1007/s00348-018-2514-3.

(4) Wang, X.; Khameneian, A.; Dice, P.; Chen, B.; Shahbakhti, M.; Naber, J. D.; Archer, C.; Qu, Q.; Glugla, C.; Huberts, G. Control-Oriented Model-Based Burn Duration and Ignition Timing Prediction with Recursive-Least-Square Based Adaptation for Closedloop Combustion Phasing Control of a Spark Ignition Engine. In *ASME 2019 Dynamic Systems and Control Conference, DSCC 2019*; American Society of Mechanical Engineers (ASME), 2019; Vol. 2. https://doi.org/10.1115/DSCC2019-9073.

(5) Ling, S.; Luo, Y.; Luan, L.; Wang, Z.; Wu, T. Inkjet Printing of Patterned Ultra-Slippery Surfaces for Planar Droplet Manipulation. *Sensors Actuators, B Chem.* **2016**, *235*, 732–738. https://doi.org/10.1016/j.snb.2016.06.120.

(6) Peppou-Chapman, S.; Neto, C. Mapping Depletion of Lubricant Films on Antibiofouling Wrinkled Slippery Surfaces. *ACS Appl. Mater. Interfaces* **2018**, *10* (39), 33669–33677.

https://doi.org/10.1021/acsami.8b11768.

(7) Palacios, J.; Hernández, J.; Gómez, P.; Zanzi, C.; López, J. Experimental Study of Splashing Patterns and the Splashing/Deposition Threshold in Drop Impacts onto Dry Smooth Solid Surfaces. *Exp. Therm. Fluid Sci.* **2013**, *44*, 571–582. https://doi.org/10.1016/j.expthermflusci.2012.08.020.

(8) Gordillo, J. M.; Riboux, G.; Quintero, E. S. A Theory on the Spreading of Impacting Droplets. *J. Fluid Mech.* **2019**, *866*, 298–315. https://doi.org/10.1017/jfm.2019.117.

(9) Josserand, C.; Ray, P.; Zaleski, S. Droplet Impact on a Thin Liquid Film: Anatomy of the Splash. *J. Fluid Mech.* **2016**, *802*, 775–805. https://doi.org/10.1017/jfm.2016.468.

(10) Zhao, Z.; Li, H.; Hu, X.; Li, A.; Cai, Z.; Huang, Z.; Su, M.; Li, F.; Li, M.; Song, Y. Steerable Droplet Bouncing for Precise Materials Transportation. *Adv. Mater. Interfaces* **2019**, *6* (21), 1901033. https://doi.org/10.1002/admi.201901033.

(11) Liu, Y.; Whyman, G.; Bormashenko, E.; Hao, C.; Wang, Z. Controlling Drop Bouncing Using Surfaces with Gradient Features. *Appl. Phys. Lett.* **2015**, *107* (5), 51604. https://doi.org/10.1063/1.4927055.

(12) Bird, J. C.; Dhiman, R.; Kwon, H. M.; Varanasi, K. K. Reducing the Contact Time of a Bouncing Drop. *Nature* **2013**, *503* (7476), 385–388. https://doi.org/10.1038/nature12740.

(13) Liu, Y.; Moevius, L.; Xu, X.; Qian, T.; Yeomans, J. M.; Wang, Z. Pancake Bouncing on Superhydrophobic Surfaces. *Nat. Phys.* **2014**, *10* (7), 515–519. https://doi.org/10.1038/nphys2980.

(14) Mokhtari, S.; Skelly, K. D.; Krull, E. A.; Coughlan, A.; Mellott, N. P.; Gong, Y.; Borges,

R.; Wren, A. W. Copper-Containing Glass Polyalkenoate Cements Based on SiO2–ZnO–CaO–SrO–P2O5 Glasses: Glass Characterization, Physical and Antibacterial Properties. *J. Mater. Sci.* **2017**, *52* (15), 8886–8903. https://doi.org/10.1007/s10853-017-0945-5.

(15) Damak, M.; Mahmoudi, S. R.; Hyder, M. N.; Varanasi, K. K. Enhancing Droplet Deposition through In-Situ Precipitation. *Nat. Commun.* **2016**, *7*. https://doi.org/10.1038/ncomms12560.

(16) Bergeron, V.; Bonn, D.; Martin, J. Y.; Vovelle, L. Controlling Droplet Deposition with Polymer Additives. *Nature* **2000**, *405* (6788), 772–775. https://doi.org/10.1038/35015525.

(17) Cheng, W. L.; Zhang, W. W.; Chen, H.; Hu, L. Spray Cooling and Flash Evaporation Cooling: The Current Development and Application. *Renewable and Sustainable Energy Reviews*. Elsevier Ltd March 1, 2016, pp 614–628. https://doi.org/10.1016/j.rser.2015.11.014.

(18) Wang, Z.; Qu, W.; Xiong, J.; Zhong, M.; Yang, Y. Investigation on Effect of Surface Properties on Droplet Impact Cooling of Cladding Surfaces. *Nucl. Eng. Technol.* **2020**, *52* (3), 508–519. https://doi.org/10.1016/j.net.2019.08.022.

(19) Yun, S. Bouncing of an Ellipsoidal Drop on a Superhydrophobic Surface. *Sci. Rep.* **2017**, *7* (1), 17699. https://doi.org/10.1038/s41598-017-18017-2.

(20) Chen, L.; Wang, Y.; Peng, X.; Zhu, Q.; Zhang, K. Impact Dynamics of Aqueous Polymer Droplets on Superhydrophobic Surfaces. *Macromolecules* **2018**, *51* (19), 7817–7827. https://doi.org/10.1021/acs.macromol.8b01589.

(21) Deegan, R. D.; Bakajin, O.; Dupont, T. F.; Huber, G.; Nagel, S. R.; Witten, T. A. Capillary

Flow as the Cause of Ring Stains from Dried Liquid Drops. *Nature* **1997**, *389* (6653), 827–829. https://doi.org/10.1038/39827.

(22) Erbil, H. Y. Evaporation of Pure Liquid Sessile and Spherical Suspended Drops: A Review. *Adv. Colloid Interface Sci.* **2012**, *170* (1–2), 67–86. https://doi.org/10.1016/j.cis.2011.12.006.

(23) Quéré, D. Wetting and Roughness. *Annu. Rev. Mater. Res.* **2008**, *38*, 71–99. https://doi.org/10.1146/annurev.matsci.38.060407.132434.

(24) Guo, Z.; Liu, W.; Su, B. L. Superhydrophobic Surfaces: From Natural to Biomimetic to Functional. *J. Colloid Interface Sci.* **2011**, *353* (2), 335–355. https://doi.org/10.1016/j.jcis.2010.08.047.

(25) Wong, T. S.; Kang, S. H.; Tang, S. K. Y.; Smythe, E. J.; Hatton, B. D.; Grinthal, A.; Aizenberg, J. Bioinspired Self-Repairing Slippery Surfaces with Pressure-Stable Omniphobicity. *Nature* **2011**, *477* (7365), 443–447. https://doi.org/10.1038/nature10447.

(26) Luo, J. T.; Geraldi, N. R.; Guan, J. H.; McHale, G.; Wells, G. G.; Fu, Y. Q. Slippery Liquid-Infused Porous Surfaces and Droplet Transportation by Surface Acoustic Waves. *Phys. Rev. Appl.* **2017**, *7* (1), 014017. https://doi.org/10.1103/PhysRevApplied.7.014017.

(27) Smith, J. D.; Dhiman, R.; Anand, S.; Reza-Garduno, E.; Cohen, R. E.; McKinley, G. H.; Varanasi, K. K. Droplet Mobility on Lubricant-Impregnated Surfaces. *Soft Matter* **2013**, *9* (6), 1772–1780. https://doi.org/10.1039/c2sm27032c.

(28) Lafuma, A.; Quéré, D. Slippery Pre-Suffused Surfaces. *Epl* **2011**, *96* (5), 56001. https://doi.org/10.1209/0295-5075/96/56001.

(29) Muschi, M.; Brudieu, B.; Teisseire, J.; Sauret, A. Drop Impact Dynamics on Slippery Liquid-Infused Porous Surfaces: Influence of Oil Thickness. *Soft Matter* **2018**, *14* (7), 1100–1107. https://doi.org/10.1039/c7sm02026k.

(30) Daniel, D.; Timonen, J. V. I.; Li, R.; Velling, S. J.; Aizenberg, J. Oleoplaning Droplets on Lubricated Surfaces. *Nat. Phys.* **2017**, *13* (10), 1020–1025. https://doi.org/10.1038/nphys4177.

(31) Keiser, A.; Keiser, L.; Clanet, C.; Quéré, D. Drop Friction on Liquid-Infused Materials. *Soft Matter* **2017**, *13* (39), 6981–6987. https://doi.org/10.1039/c7sm01226h.

(32) Hui Guan, J.; Ruiz-Gutiérrez, É.; Xu, B. Bin; Wood, D.; McHale, G.; Ledesma-Aguilar, R.; Wells, G. G. Drop Transport and Positioning on Lubricant-Impregnated Surfaces. *Soft Matter* **2017**, *13* (18), 3404–3410. https://doi.org/10.1039/c7sm00290d.

(33) Lee, C.; Kim, H.; Nam, Y. Drop Impact Dynamics on Oil-Infused Nanostructured Surfaces. *Langmuir* **2014**, *30* (28), 8400–8407. https://doi.org/10.1021/la501341x.

(34) Hao, C.; Li, J.; Liu, Y.; Zhou, X.; Liu, Y.; Liu, R.; Che, L.; Zhou, W.; Sun, D.; Li, L.; Xu, L.; Wang, Z. Superhydrophobic-like Tunable Droplet Bouncing on Slippery Liquid Interfaces. *Nat. Commun.* **2015**, *6*. https://doi.org/10.1038/ncomms8986.

(35) Kim, J. H.; Rothstein, J. P. Droplet Impact Dynamics on Lubricant-Infused Superhydrophobic Surfaces: The Role of Viscosity Ratio. *Langmuir* **2016**, *32* (40), 10166–10176. https://doi.org/10.1021/acs.langmuir.6b01994.

(36) Kim, S.; Wang, T.; Zhang, L.; Jiang, Y. Droplet Impacting Dynamics on Wettable, Rough and Slippery Oil-Infuse Surfaces. *J. Mech. Sci. Technol.* **2020**, *34* (1), 219–228.

https://doi.org/10.1007/s12206-019-1223-z.

(37) Baek, S.; Yong, K. Impact Dynamics on SLIPS: Effects of Liquid Droplet's Surface Tension and Viscosity. *Appl. Surf. Sci.* **2020**, *506*, 144689. https://doi.org/10.1016/j.apsusc.2019.144689.

(38) Salipante, P. F.; Vlahovska, P. M. Electrohydrodynamics of Drops in Strong Uniform Dc Electric Fields. *Phys. Fluids* **2010**, *22* (11), 112110. https://doi.org/10.1063/1.3507919.

(39) Zhang, H.; Zhang, X.; Yi, X.; He, F.; Niu, F.; Hao, P. Dynamic Behaviors of Droplets Impacting on Ultrasonically Vibrating Surfaces. *Exp. Therm. Fluid Sci.* **2020**, *112* (June 2019), 110019. https://doi.org/10.1016/j.expthermflusci.2019.110019.

(40) Weisensee, P. B.; Ma, J.; Shin, Y. H.; Tian, J.; Chang, Y.; King, W. P.; Miljkovic, N. Droplet Impact on Vibrating Superhydrophobic Surfaces. *Phys. Rev. Fluids* **2017**, *2* (10), 103601. https://doi.org/10.1103/PhysRevFluids.2.103601.

(41) Soltani-Kordshuli, F.; Eslamian, M. Impact Dynamics and Deposition of Pristine and Graphene-Doped PEDOT:PSS Polymeric Droplets on Stationary and Vibrating Substrates. *Exp. Therm. Fluid Sci.* **2017**, *89*, 238–248. https://doi.org/10.1016/j.expthermflusci.2017.08.019.

(42) Fu, Y. Q.; Luo, J. K.; Nguyen, N. T.; Walton, A. J.; Flewitt, A. J.; Zu, X. T.; Li, Y.; McHale, G.; Matthews, A.; Iborra, E.; Du, H.; Milne, W. I. Advances in Piezoelectric Thin Films for Acoustic Biosensors, Acoustofluidics and Lab-on-Chip Applications. *Prog. Mater. Sci.* **2017**, *89*, 31–91. https://doi.org/10.1016/j.pmatsci.2017.04.006.

(43) Li, J.; Xu, N.; Dong, L.; Li, J.; Biroun, M. H.; Tao, R.; Torun, H.; Xu, N.; Rahmati, M.; Li,

Y.; Fu, Y.; Tao, R.; Fu, C.; Luo, J.; Wang, Y.; Xie, J.; Gibson, D. Wide Range of Droplet Jetting Angles by Thin-Film Based Surface Acoustic Waves. *J. Phys. D. Appl. Phys.* **2020**, *53* (35), 355402. https://doi.org/10.1088/1361-6463/ab8f50.

(44) Biroun, M. H.; Rahmati, M. T.; Jangi, M.; Tao, R.; Chen, B. X.; Fu, Y. Q. Computational and Experimental Analysis of Droplet Transportation/Jetting Behaviours Driven by Thin Film Surface Acoustic Waves. *Sensors Actuators, A Phys.* **2019**, *299*, 111624. https://doi.org/10.1016/j.sna.2019.111624.

(45) Wang, J.; Hu, H.; Ye, A.; Chen, J.; Zhang, P. Experimental Investigation of Surface Acoustic Wave Atomization. *Sensors Actuators, A Phys.* **2016**, *238*, 1–7. https://doi.org/10.1016/j.sna.2015.11.027.

(46) Lim, H.; Back, S. M.; Choi, H.; Nam, J. Acoustic Mixing in a Dome-Shaped Chamber-Based SAW (DC-SAW) Device. *Lab Chip* **2020**, *20* (1), 120–125. https://doi.org/10.1039/c9lc00820a.

(47) Tao, R.; Wang, W. B.; Luo, J. T.; Ahmad Hasan, S.; Torun, H.; Canyelles-Pericas, P.; Zhou, J.; Xuan, W. P.; Cooke, M. D.; Gibson, D.; Wu, Q.; Ng, W. P.; Luo, J. K.; Fu, Y. Q. Thin Film Flexible/Bendable Acoustic Wave Devices: Evolution, Hybridization and Decoupling of Multiple Acoustic Wave Modes. *Surf. Coatings Technol.* **2019**, *357*, 587–594. https://doi.org/10.1016/j.surfcoat.2018.10.042.

(48) Biroun, M. H.; Rahmati, M.; Tao, R.; Torun, H.; Jangi, M.; Fu, Y. Dynamic Behavior of Droplet Impact on Inclined Surfaces with Acoustic Waves. *Langmuir* **2020**, *36* (34), 10175–10186. https://doi.org/10.1021/acs.langmuir.0c01628.

(49) Biroun, M. H.; Li, J.; Tao, R.; Rahmati, M.; McHale, G.; Dong, L.; Jangi, M.; Torun, H.; Fu, Y. Q. Acoustic Waves for Active Reduction of Contact Time in Droplet Impact. *Phys. Rev. Appl.* **2020**, *14* (2), 1–18. https://doi.org/10.1103/PhysRevApplied.14.024029.

(50) Geraldi, N. R.; Guan, J. H.; Dodd, L. E.; Maiello, P.; Xu, B. B.; Wood, D.; Newton, M. I.; Wells, G. G.; McHale, G. Double-Sided Slippery Liquid-Infused Porous Materials Using Conformable Mesh. *Sci. Rep.* **2019**, *9* (1), 1–8. https://doi.org/10.1038/s41598-019-49887-3.

(51) Orme, B. V.; McHale, G.; Ledesma-Aguilar, R.; Wells, G. G. Droplet Retention and Shedding on Slippery Substrates. *Langmuir* **2019**, *35* (28), 9146–9151. https://doi.org/10.1021/acs.langmuir.9b00931.

(52) Landau, L.; Levich, B. Dragging of a Liquid by a Moving Plate. *Dyn. Curved Front.* **1988**, *17*, 141–153. https://doi.org/10.1016/b978-0-08-092523-3.50016-2.

(53) Seiwert, J.; Clanet, C.; Quéré, D. Coating of a Textured Solid. *J. Fluid Mech.* **2011**, *669*, 55–63. https://doi.org/10.1017/S0022112010005951.

(54) McHale, G.; Orme, B. V.; Wells, G. G.; Ledesma-Aguilar, R. Apparent Contact Angles on Lubricant-Impregnated Surfaces/SLIPS: From Superhydrophobicity to Electrowetting. *Langmuir* **2019**, *35* (11), 4197–4204. https://doi.org/10.1021/acs.langmuir.8b04136.

(55) Tao, R.; Mchale, G.; Reboud, J.; Cooper, J. M.; Torun, H.; Luo, J. T.; Luo, J.; Yang, X.; Zhou, J.; Canyelles-Pericas, P.; Wu, Q.; Fu, Y. Hierarchical Nanotexturing Enables Acoustofluidics on Slippery yet Sticky, Flexible Surfaces. *Nano Lett.* **2020**, *20* (5), 3263–3270. https://doi.org/10.1021/acs.nanolett.0c00005.

(56) Cao, M.; Guo, D.; Yu, C.; Li, K.; Liu, M.; Jiang, L. Water-Repellent Properties of Superhydrophobic and Lubricant-Infused "Slippery" Surfaces: A Brief Study on the Functions and Applications. *ACS Appl. Mater. Interfaces* **2016**, *8* (6), 3615–3623. https://doi.org/10.1021/acsami.5b07881.

(57) Yang, Q.; Luo, Z.; Jiang, F.; Luo, Y.; Tan, S.; Lu, Z.; Zhang, Z.; Liu, W. Air Cushion Convection Inhibiting Icing of Self-Cleaning Surfaces. *ACS Appl. Mater. Interfaces* **2016**, *8* (42), 29169–29178. https://doi.org/10.1021/acsami.6b10165.

(58) Launay, G.; Sadullah, M. S.; McHale, G.; Ledesma-Aguilar, R.; Kusumaatmaja, H.; Wells, G. G. Self-Propelled Droplet Transport on Shaped-Liquid Surfaces. *Sci Rep* **2019**, 10, 1–23. https://doi.org/10.1038/s41598-020-70988-x

(59) Liu, Z.; Zhan, J.; Fard, M.; Davy, J. L. Acoustic Properties of Multilayer Sound Absorbers with a 3D Printed Micro-Perforated Panel. *Appl. Acoust.* **2017**, *121*, 25–32. https://doi.org/10.1016/j.apacoust.2017.01.032.

(60) Johnson, D. L.; Koplik, J.; Dashen, R. Theory of Dynamic Permeability and Tortuosity in Fluid Saturated Porous Media. *J. Fluid Mech.* **1987**, *176*, 379–402. https://doi.org/10.1017/S0022112087000727.

(61) Liu, Z.; Fard, M.; Jazar, R.; Cui, X. Development of an Acoustic Material Database for Vehicle Interior Trims. *SAE Tech. Pap.* **2015**, *2015-March* (March). https://doi.org/10.4271/2015-01-0046.

(62) Du Plessis, J. P.; Masliyah, J. H. Flow through Isotropic Granular Porous Media. *Transp. Porous Media* **1991**, *6* (3), 207–221. https://doi.org/10.1007/BF00208950.

(63) Kinsler, L.; Frey, A.; Coppens, A.; Sanders, J. *Fundamentals Of Acoustics*, 3rd ed.; Wiley: New York, 1982.

(64) Sudeepthi, A.; Yeo, L.; Sen, A. K. Cassie-Wenzel Wetting Transition on Nanostructured Superhydrophobic Surfaces Induced by Surface Acoustic Waves. *Appl. Phys. Lett.* **2020**, *116* (9), 1–6. https://doi.org/10.1063/1.5145282.

(65) Liu, Y.; Yan, X.; Wang, Z. Droplet Dynamics on Slippery Surfaces: Small Droplet, Big Impact. *Biosurface and Biotribology* **2019**, *5* (2), 35–45. https://doi.org/10.1049/bsbt.2019.0004.

(66) Alghane, M.; Fu, Y. Q.; Chen, B. X.; Li, Y.; Desmulliez, M. P. Y.; Walton, A. J. Frequency Effect on Streaming Phenomenon Induced by Rayleigh Surface Acoustic Wave in Microdroplets. *J. Appl. Phys.* **2012**, *112* (8). https://doi.org/10.1063/1.4758282.

(67) Connacher, W.; Zhang, N.; Huang, A.; Mei, J.; Zhang, S.; Gopesh, T.; Friend, J. Micro/Nano Acoustofluidics: Materials, Phenomena, Design, Devices, and Applications. *Lab Chip* **2018**, *18* (14), 1952–1996. https://doi.org/10.1039/c8lc00112j.

TOC Graphic

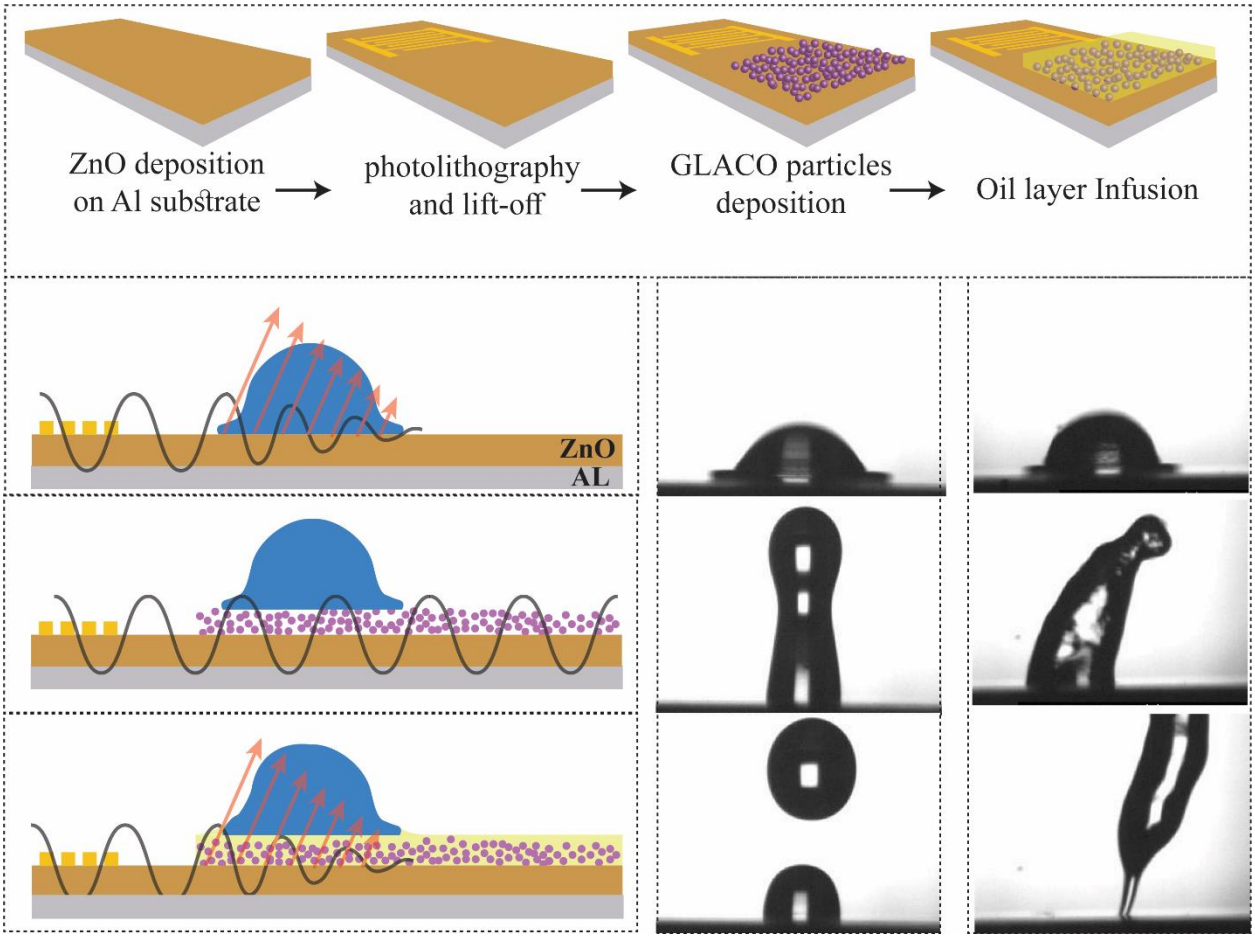
ZnO deposition on Al substrate
photolithography and lift-off
GLACO particles deposition
Oil layer Infusion
ZnO
AL